Article

Bio-Inspired Deep-CNN Pipeline for Skin Cancer Early Diagnosis

Francesco Rundo [1,]*[ID]**, Giuseppe Luigi Banna** [2] **and Sabrina Conoci** [1][ID]

[1] STMicroelectronics ADG—Central R&D, Stradale Primosole 50, 95121 Catania, Italy
[2] Division of Medical Oncology, Cannizzaro Hospital, 95126 Catania, Italy
* Correspondence: francesco.rundo@st.com; Tel.: +39-095-7404566

Abstract: Skin cancer is the most common type of cancer, as also among the riskiest in the medical oncology field. Skin cancer is more common in people who work or practice outdoor sports and those that expose themselves to the sun. It may also develop years after radiographic therapy or exposure to substances that cause cancer (e.g., arsenic ingestion). Numerous tumors can affect the skin, which is the largest organ in our body and is made up of three layers: the epidermis (superficial layer), the dermis (middle layer) and the subcutaneous tissue (deep layer). The epidermis is formed by different types of cells: melanocytes, which have the task of producing melanin (a pigment that protects against the damaging effects of sunlight), and the more numerous keratinocytes. The keratinocytes of the deepest layer are called basal cells and can give rise to basal cell carcinomas. We are interested in types of skin cancer that originate from melanocytes, i.e., the so-called melanomas, because it is the most aggressive. The dermatologist, during a complete visit, evaluates the personal and family history of the patient and carries out an accurate visual examination of the skin, thanks to the use of epi-luminescence (or dermoscopy), a special technique for enlarging and illuminating the skin. This paper mentions one of the most widely used diagnostic methods due to its simplicity and validity—the ABCDE method (Asymmetry, edge irregularity, Color Variegation, Diameter, Evolution). This methodology, based on "visual" investigation by the dermatologist and/or oncologist, has the advantage of not being invasive and quite easy to perform. This approach is affected by the opinion of who (physicians) applies it. For this reason, certain diagnosis of cancer is made, however, only with a biopsy, a procedure during which a portion of tissue is taken and then analyzed under a microscope. Obviously, this is particularly invasive for the patient. The authors of this article have analyzed the development of a method that obtains with good accuracy the early diagnosis of skin neoplasms using non-invasive, but at the same time, robust methodologies. To this end, the authors propose the adoption of a deep learning pipeline based on morphological analysis of the skin lesion. The results obtained and compared with previous approaches confirm the good performance of the proposed pipeline.

Keywords: deep learning; skin cancer; melanoma; STM32

1. Introduction

The stage of skin cancer indicates how widespread the disease is in the body and is a very important parameter for determining prognosis and deciding on the type of treatment to be undertaken. Therefore, diagnosis and relative early staging are of fundamental importance to increase a patient's chances of survival. Basal cell and spino-cellular carcinomas, unlike other skin tumors such as melanoma, metastasize only in rare cases and many years after their appearance. As a result, they are usually removed when they are still located. In persons with immune system issues, spino-cellular carcinomas can be at high risk of metastasis and for this we proceed with staging with the TNM system: tumors can be classified into four stages (I, II, III and IV) based on the size and position of

the disease (T), involvement of lymph nodes (N) and presence of metastases (M). It is clear, therefore, that the search for an efficient and accurate approach that allows dermatologists and/or oncologists to quickly discriminate skin lesion (the so-called "nevus") suspicions (which therefore deserve further investigation) is a subject of considerable attention by researchers in the medical field. Basal cell and spino-cellular carcinomas, if treated in the initial phases, recover in almost all cases and can often be treated completely, thanks to surgery and/or local treatments. Therefore, surgery is generally the first choice treatment for these tumors. Radiotherapy and systemic chemotherapy (to the whole body) are not used very often for skin carcinomas: chemotherapy is useful in cases where the tumor has reached lymph nodes. Therefore, much emphasis is placed on early diagnosis, especially for the most aggressive histology of melanoma.

Among the commonly used methods for early diagnosis of skin tumors is the "ABCDE Method"; based on the abbreviation, the following nevus characteristics are monitored: Asymmetry, Borders, variegation of the Color, Diameter, Evolution of the lesion cuts. Basically, a physician who applies the ABCDE criterion in the analysis of a skin lesion performs a visual statistical evaluation of the nevus based on the heuristic (and experience-based) evaluation of the characteristics mentioned. Clearly, this strategy suffers from the subjectivity of the clinician or low sensitivity and specificity. Consequently, analysis by the ABCDE method is followed by the necessary biopsy confirmation that often, however, belies the apparent oncological risk that instead the dermatologist had estimated by means of the ABCDE analysis. In order to correctly address this issue, the authors propose an automatic pipeline discrimination system based on the analysis of dermoscopic images so as to classify the low-risk lesion (benign lesions or low risk of oncological progression) from those at high risk (high risk of oncological progression), trying to find a good trade-off between sensitivity and specificity.

Scientific research is making significant progress in the aspect of early nevus diagnosis. A method that currently shows itself to be particularly promising is the so-called "ex vivo confocal microscopy" (performed on excised tissue), which allows us to anticipate the time taken for standard histological analyzes, which is about 10 days. The specificity—the ability to exclude the presence of the disease—of this method is particularly high. Thus, this new method allows to intervene with the biopsy only if necessary and not as a precaution in case of suspected malignancy. However, methods based on recent deep learning techniques continue to be much investigated by researchers around the world.

The authors recently developed two different implementations of deep systems for skin lesion discrimination [1,2]. The obtained results are promising. A subsequent extension of the proposed approach is described in [3] and in which performances have been strongly increased, thanks to revision of the hand-crafted image features, adopted together with the use of Stacked Deep Autoencoder as classifiers of such features. All the algorithmic versions proposed by the authors in the previous referenced works have been successfully validated using the public dataset (containing a set of dermoscopic images of benign and malignant nevi) called PH^2 [4].

However, in the scientific literature, different algorithmic approaches have been proposed for the early and robust diagnosis of skin cancer. Among these, it is worth mentioning methods based on classical pattern recognition techniques combined with the statistical study of dermoscopic images [5,6]. In [6–9], some methods for classifying skin cancer are described, which are based on the adaptive analysis of the so-called global and local characteristics of lesions. Using soft computing techniques, the authors of these pipelines have successfully discriminated skin lesions by post-processing these features. Also the use of clustering methods based on Support Vector Machines (SVM), Artificial Neural Networks (ANNs), K-closer, Naive-Bayes Algorithm have shown remarkable discriminative abilities, compared to the classical methods based on the search for specific patterns in dermoscopic images [8,9]. A very promising approach has been proposed in [7], in which the features of ad hoc hand-crafted dermoscopic image features are combined with an in-depth learning algorithm capable of extracting additional learned functions, as well as classifying the entire set of features with respect to the characterization of benign versus malignant lesions. However, the analysis of the results obtained in [7] shows a fairly low sensitivity/specificity ratio. In [8], the authors propose an interesting novel

multiple convolution neural network model (MCNN) to classify different disease types in dermoscopic images, where several models were trained separately using an additive sample learning strategy. The results are promising, as confirmed by authors in [8]. An interesting consideration was made by such authors in [9] in which the skin lesion images dataset was augmented before it is used in the deep learning pipeline. The image dataset augmentation showed an interesting performance increase with respect to the same approach applied in the same dataset without augmentation pre-processing. More details are provided in [9].

The authors intend to propose an innovative method of nevus discrimination for the early diagnosis of high-risk malignancy lesions (with particular attention to the histology called melanoma as the most aggressive). Considering that melanoma originates in the melanocytic cells of the epidermis, we characterized the proposed hand-crafted features that were particularly attentive to the superficial melanocytic distribution of the nevus. In fact, we designed ad-hoc hand-crafted image features that allow us to characterize the self-similarity of melanocytic cells in addition to the degree of symmetry and regularity of the edges of the lesion of the skin, as specified in the next paragraphs. In this way, we bio-inspired the proposed algorithm, since the characterization of the nevus is correlated to the analytical modeling of the physical properties of the melanocytic cells of the analyzed lesion. Moreover, the algorithmic part linked to the use of Cellular Neural Networks (CNNs) was hypothesized to analyze each pixel of the lesion (which groups several melanocytic cells) by means of the processing defined by the suitably configured CNNs' cell state equation. Therefore, each CNN's setup allows the characterization of a specific morphological feature of the analyzed lesion, thus enabling the discriminator system based on convolutive multi-level deep architecture to learn these morphological features and from these to provide an internal functional mapping useful for classifying the analyzed skin lesion. The proposed method will be compared with methods present in scientific literature and previous algorithmic versions proposed by the authors [1–3]. In order to guarantee a robust basis of comparison, it was decided to apply and validate the proposed pipeline in the same database of dermoscopic images, i.e., the PH^2 database [4].

2. Materials and Methods

Figure 1 shows the proposed pipeline. Each block is detailed in the following paragraphs. The pipeline proposed here aims to analyze the dermoscopic image of the nevus generating features that are characteristic of the lesion of the skin, which allows the convolutional classification system to characterize the high risk of oncological progression or confirm its benignity. In this way, we want to provide physicians with a practical and innovative tool that allows them to diagnose with sufficient evidence the neoplastic progression of a new growth of skin.
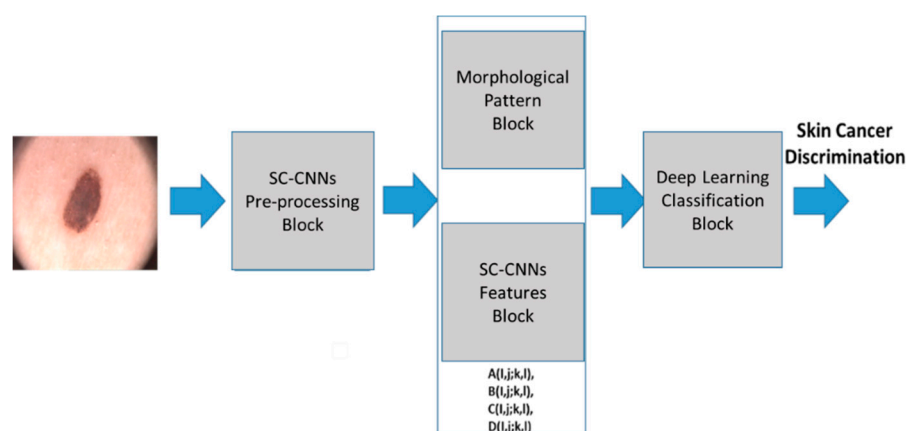

Figure 1. The proposed bio-inspired skin lesion discrimination pipeline.

2.1. SC-CNNs Pre-Processing Block

The input dermoscopy lesion image $D(x,y)$ is usually a simple RGB colour image acquired by classical medical optical dermatoscope.

Dermatoscopy, dermoscopy or epiluminescence, is a non-invasive technique aimed at the early diagnosis of melanoma based on an optical instrument called a dermatoscope, which allows to observe sub-cutaneous patterns not visible to the naked eye, favoring their recognition.

The optical dermatoscope is a small manual tool based on a lens, able to provide magnifications mainly between 10 and 20 times, specially illuminated with incident light. It is now demonstrated how dermoscopy increases the diagnostic sensitivity for melanoma compared to simple vision with the naked eye of 20–30%, allowing early diagnosis. Experiences over the last decade have made it possible to extend the application of this diagnostic technique to non-pigmented skin lesions. Today dermatoscopy is particularly effective in the recognition of non-melanocytic skin tumors such as melanoma, basal cell carcinoma and Bowen's disease and of other cutaneous neo-formations such as seborrheic keratoses, actinic keratoses, dermatofibroma, and clear cell acanthoma. Figure 2 shows a classical dermoscopy image of a nevus. We are interested in a method that allows us to discriminate oncologically the lesion of the skin using a low computational complexity method.
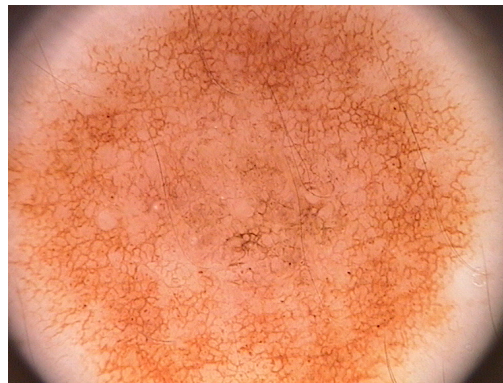
Figure 2. A typical dermoscopy image of a skin nevus.

For this reason, the proposed pipeline will process the gray-level component of the starting dermoscopic RGB colour image. To do that, the source dermoscopic colour images are converted into YCbCr format [10–12] from which we will estract only the luminance component (gray levels image). We denoted this gray-levels image as $Y_p(x,y)$. It is fed as "input" and "state" to a State-Controlled Cellular Neural Networks (SC-CNNs) 2D matrix having a size equal to the source image $Y_p(x,y)$ i.e., $m \times n$.

The first version of the Cellular Neural (or Nonlinear) Network (CNN) was proposed by L.O Chua and L. Yang [13]. The CNNs can be defined as a high speed, local interconnected computing array of analog processors. The CNN dynamic is defined through so-called cloning template matrixes. The CNN cells interact with each other within their neighbourhood, defined by a heuristic radius.

Each CNN cell has an input, a state, and an output, which is correlated to the state (usually by means of Pieweise Linear (PWL) function). The CNN can be implemented both in digital (trough FPGA technology) and analog (VLSI or UVLSI technology) for which it is able to perform high speed "near real-time" computations. Some stability results by means of Lyapunov theorems and consideration about the dynamics of the CNNs can be found in [13]. Several extensions of classical CNN have been reported in the literature, among which it is worth mentioning the so-called State-Controlled CNNs introduced (SC-CNNs) by Arena et al. in [14]. This model directly explicates the dependency of dynamic evolution of the cell to the "state" of the single cell. We refer to SC-CNNs in the following mathematical formulations. By assigning each normalized gray-level lesion image $Y_p(x,y)$ (of size $m \times n$) to input and state of the SC-CNNs, several image processing tasks may be performed according

to the defined cloning templates instructions [14]. Equation (1) defines the state equation of a $(m \times n)$ SC-CNNs. $Nr(i,j)$ represents the neighbourhood of each cell $C(i,j)$ with radius r; x_{ij} represents the state, y_{ij} the output (mapped to the state x_{ij} by means of a classical PWL equation), and u_{ij} the input of the cell $C(i,j)$. The cloning templates suitable to define the dynamic of the SC-CNNs are respectively $A(i,j;k,l)$, $B(i,j;k,l)$, $C(i,j;k,l)$, and the constant bias I. The coefficients C and R_x are correlated to the capacitor and resistance of the analog circuit used to implement the single SC-CNNs cell [13,14].

$$
\begin{aligned}
C\frac{dx_{ij}(t)}{dt} = & -\frac{1}{R_x}x_{ij} + \sum_{C(k,l)\in N_r(i,j)} A(i,j;k,l)y_{kl}(t) + \sum_{C(k,l)\in N_r(i,j)} B(i,j;k,l)u_{kl}(t) \\
& + \sum_{C(k,l)\in N_r(i,j)} C(i,j;k,l)x_{kl}(t) + I \\
& (1 \le i \le M, 1 \le j \le N) \\
& y_{ij}(t) = \tfrac{1}{2}\left(\left|x_{ij}(t)+1\right| - \left|x_{ij}(t)-1\right|\right) \\
N_r(i,j) = & \left\{C_r(k,l); \left(\max\left(|k-i|,|i-j|\right)\right) \le r, 1 \le k \le M, 1 \le l \le N\right\}
\end{aligned}
$$
(1)

As anticipated, the SC-CNNs compared to the classical CNNs model introduced by Chua and Yang make it possible to explain the direct dependence between the state of the cell with that of the adjacent cells belonging to its own neighborhood. In this way, we were able to characterize different image processing tasks with respect to the same executable using the CNN model originally proposed by Chua and Yang. Through SC-CNNs, we can better exploit the dependence between the dynamics of the state of individual cells in the network. In this way, considering that the intensity of the single pixel of the dermoscopic image is associated with the state of the single cell of the SC-CNNs, through the appropriate configurations of the cloning templates, we are able to highlight certain morphological characteristics of the nevus or eliminate others.

Before processing the acquired pre-processed nevus image, it is important to segment the Region of Interest (ROI) of the image (i.e., the nevus) with respect to background (skin). Considering that skin lesion segmentation is another issue currently under investigation by the authors, we decided to focus on the only objective of discriminating against skin lesions and for this reason we used a segmentation mask provided by the dermoscopy images database we used for validating the proposed approach i.e., the PH^2 database [2].

The SC-CNNs pre-processing pipeline is detailed in Figure 3, while Equation (2) reports the setup of the used pre-processing cloning templates [2,15].

$$
A = \begin{bmatrix} 0 & 0 & 0 \\ 0 & 0 & 0 \\ 0 & 0 & 0 \end{bmatrix}; B = \begin{bmatrix} 2.8 & 0.20 & 0.20 \\ 0.20 & 2.71 & 0.20 \\ 2.71 & 0.20 & 0.20 \end{bmatrix}; C = \begin{bmatrix} 0 & 0 & 0 \\ 0 & 0 & 0 \\ 0 & 0 & 0 \end{bmatrix}; I = 0.65
$$
(2)

Figure 3. The pre-processing block based on SC-CNNs.

The cloning templates in (2) are useful to configure SC-CNNs in order to perform ad-hoc adaptive time-transient image stabilization (motion artifacts, dermo-gel, etc.). The cloning templates' setup used in (2) improves stabilization with respect to the previous version used in [1–3]. The dermoscopy gray level image processed by SC-CNNs is denoted as $Y_{SCC}(x,y)$. Figure 4a–d show the mask and output images related to the SC-CNN pre-processing task.
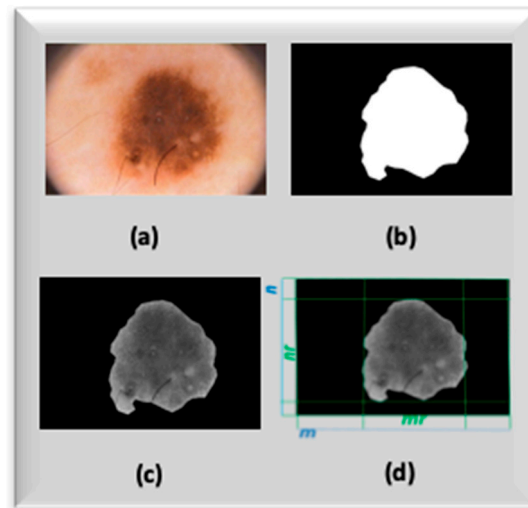
Figure 4. (**a**) Original RGB dermoscopy image, (**b**) image-mask provided by PH^2 database, (**c**) SC-CNNs pre-processed image, (**d**) segmented SC-CNNs pre-processed image with details.

2.2. Morphological Pattern and SC-CNNs Features Block

The aim of this block is to provide a mathematical representation of the ABCDE rule aforementioned in this paper. The mathematical modeling of the ABCDE heuristic rule is obtained by using a combination of hand-crafted image features with Deep Learning generated features. Preliminarily, the proposed set of hand crafted image features is analyzed. The proposed image features are re-scaled via logarithmic function with the aim to reduce the range of their variability. We propose the main representative subset of the hand-crafted features we developed in our previous pipeline [3]. We added new features and replaced others, as we have noted that the overal performance of the method was improved. In detail, we added the 7-th order moment (feature F_{11}) and a modified version of the "cosine similarity" feature (F_{16}) with respect to the same used in previous work [3]. We dropped features F_{14}, F_{18}–F_{21} proposed in the previous version of the pipeline [3], as they do not bring any improvement in the overall discrimination performance of the algorithm herein described. We proceed in the description of the used features in the shown algorithm by indicating with *nr* and *mr* the dimension of the bounding box enclosing the ROI (Figure 4d), respectively, while *p(i,j)* represents the gray-level intensity of each pre-processed image pixel:

$$F_1 = \log\left(\frac{1}{m \cdot n} \sum_{i=1}^{mr} \sum_{j=1}^{nr} p(i,j)\right) \tag{3}$$

$$F_2 = log\left(\frac{1}{mr \cdot nr} \sum_{i=1}^{m} \sum_{j=1}^{n} \left(\left|p(i,j) - F_1\right|\right)\right) \tag{4}$$

$$F_3 = \log\left(\frac{1}{mr \cdot nr} \sum_{i=1}^{m} \sum_{j=1}^{n} \left(p(i,j) - F_1\right)^2\right) \tag{5}$$

$$F_4 = \sqrt{|F_3|} \tag{6}$$

$$F_5 = \log\left(\frac{\pi}{2} \cdot \frac{1}{m \cdot n} \sum_{i=1}^{m} \sum_{j=1}^{n} \left(\left|p(i,j) - F_1\right|\right)\right) \tag{7}$$

$$F_6 = \log\left(\sqrt{\left|F_3 - (F_6)^2\right|}\right) \tag{8}$$

$$F_7 = \log\left(\frac{1}{mr \cdot nr} \sum_{i=1}^{m} \sum_{j=1}^{n} \left(\frac{|p(i,j) - F_1|}{F_4}\right)^3\right) \tag{9}$$
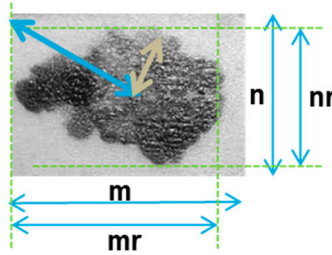
$$F_8 = \log\left(\frac{1}{mr \cdot nr} \sum_{i=1}^{m} \sum_{j=1}^{n} \left(\left|i - \frac{m}{2}\right|\right) \cdot \left(\left|j - \frac{n}{2}\right|\right)\left(\frac{p(i,j) - F_1}{F_4}\right)^4\right) \tag{10}$$

$$F_9 = \log\left(\frac{1}{mr \cdot nr} \sum_{i=1}^{m} \sum_{j=1}^{n} \left(\left|i - \frac{m}{2}\right|\right) \cdot \left(\left|j - \frac{n}{2}\right|\right)\left(\frac{|p(i,j) - F_1|}{F_4}\right)^5\right) \tag{11}$$

$$F_{10} = \log\left(\frac{1}{mr \cdot nr} \sum_{i=1}^{m} \sum_{j=1}^{n} \left(\left|i - \frac{m}{2}\right|\right) \cdot \left(\left|j - \frac{n}{2}\right|\right)\left(\frac{p(i,j) - F_1}{F_4}\right)^6\right) \tag{12}$$

$$F_{11} = \log\left(\frac{1}{mr \cdot nr} \sum_{i=1}^{m} \sum_{j=1}^{n} \left(\left|i - \frac{m}{2}\right|\right) \cdot \left(\left|j - \frac{n}{2}\right|\right)\left(\frac{p(i,j) - F_1}{F_4}\right)^7\right) \tag{13}$$

$$F_{12} = \log\left(\frac{1}{mr \cdot nr} \sum_{i=1}^{m} \sum_{j=1}^{n} \left(\left|i - \frac{m}{2}\right|\left|j - \frac{n}{2}\right| \cdot (p(i,j))^2\right)\right) \tag{14}$$

The following Figure 5 shows the contribution of the hand-crafted feature F_{12} for the right characterization of melanocyte distribution over the skin epidermis as well as "ad-hoc" measure of nevus area/dermoscopy area ratio (fixed input dermo-image size):

Figure 5. Graphical representation of the nevus image processing done by feature F_{12}.

$$F_{13} = \log\left(\frac{1}{mr \cdot nr} \sum_{i=1}^{m} \sum_{j=1}^{n} \left(\left|i - \frac{m}{2}\right| \cdot \left|j - \frac{n}{2}\right| \cdot (p(i,j) \cdot (i - j)^2)\right)\right) \tag{15}$$

$$F_{14} = \log\left(\frac{1}{mr \cdot nr} \sum_{i=1}^{m-k} \sum_{j=1}^{n-k} \left(\left|i - \frac{m}{2}\right| \cdot \left|j - \frac{n}{2}\right| \cdot (|p(i,j) - p(i+k,j+k)|)\right)\right) \tag{16}$$

$$F_{15} = log\left(m \cdot n \cdot \frac{1}{12} \cdot \frac{1}{mr \cdot nr} \cdot \left((F_7)^4 + \left(\frac{1}{16} \cdot (F_8 - 3)^2\right)\right)\right) \tag{17}$$

$$F_{16} = \log\left(\frac{1}{mr \cdot nr} \cdot \left(\sum_{i=1}^{round(\frac{m}{2})} \sum_{j=1}^{n} \left(\left|i - \frac{m}{2}\right| \cdot \left|j - \frac{n}{2}\right|\right) \cdot \frac{|p(i,j) - p(i+1,j)| \cdot (i-j)^2}{\sqrt{(p(i,j))^2 + (p(i+1,j))^2}}\right) + \left(\sum_{i=1}^{m} \sum_{j=1}^{round(\frac{n}{2})} \left(\left|i - \frac{m}{2}\right| \cdot \left|j - \frac{n}{2}\right|\right) \cdot \frac{|p(i,j) - p(i,j+1)| \cdot (i-j)^2}{\sqrt{(p(i,j))^2 + (p(i,j+1))^2}}\right)\right)\right) \tag{18}$$

The following Figure 6 shows the contribution of the hand-crafted feature F_{16} for the right characterization of "similarity and symmetry" of the skin lesion i.e., weighted average measure of nevus asymmetry ("A" of the ABCDE rule) with specific weights for border part of nevus; specific

weighted average measure of symmetry ratio between the borders and nevus core and, finally, specific weighted measure of symmetry distribution of the near pixels of nevus segmented dermo-image:
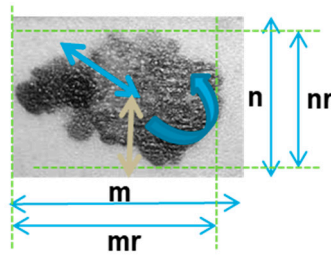
Figure 6. Graphical representation of the nevus image processing made by feature F_{16}.

As said, the feature F_1 to F_6 are classical statistical features suitable to characterize melanocyte distribution in terms of a statistical process. The features F_7 to F_{15} are a modified version of statistical moments, such that they are useful to characterize the dynamic evolution (borders, radius, colour and asimmetry) of the nevus. The feature F_{16} is a modified version of the so-called "cosine similarity", used to analyze the intrinsic similarity and symmetry of the nevus, while the feature F_{15} is a modified advanced version of the "Jarque-Bera index", which is able to point-out kurtosis and skewness of time-series and is often applied in the field of financial markets. In the proposed work, we adapted the Jarque-Bera index to 2D image analysis with regards to the kurtosis and skewness features for the analyzed pre-processed dermoscopic image. We used $k = 9$ in Equation (16).

In order to improve the performance of the previous version of the proposed pipeline, the authors analyzed features obtained by means of a modified version of SC-CNNs i.e., the so-called NonLinear SC-CNNs (NLSC-CNNs). Formally, an NLSC-CNNs can be mathematically represented as follows:

$$
\begin{aligned}
C\frac{dx_{ij}(t)}{dt} = & -\frac{1}{R_x}x_{ij} + \sum_{C(k,l)\in N_r(i,j)} A(i,j;k,l)y_{kl}(t) + \sum_{C(k,l)\in N_r(i,j)} B(i,j;k,l)u_{kl}(t) \\
& + \sum_{C(k,l)\in N_r(i,j)} C(i,j;k,l)x_{kl}(t) \\
& + \sum_{C(k,l)\in N_r(i,j)} D(i,j;k,l)\big(y_{ij}(t),y_{kl}(t)\big) + I \\
& (1 \leq i \leq M, 1 \leq j \leq N) \\
& y_{ij}(t) = \tfrac{1}{2}\big(\big|x_{ij}(t)+1\big|-\big|x_{ij}(t)-1\big|\big)
\end{aligned}
\tag{19}
$$

A nonlinear template $D(i,j;k,l)$ has been added to the model reported in Equation (1) in order to exploit the nonlinearity relationship between the outputs of single cell with its neighborhood. The NLSC-CNNs allow to characterize the dependence between the output of the single cell with those of the cells belonging to its neighborhood. In this way, it was possible to highlight the dynamic correlation between the processing of individual pixel that contain, as mentioned, groups of melanocytic cells. In this way, through the designed NLSC-CNNs, we can study the morphological dynamics of melanocytic cells (output of the single cell of the NLSC-CNNs architecture) for each type of processing defined by the designed cloning template. This result would not have been possible with the CNNs model proposed by Chua and Yang nor with that defined by classic SC-CNNs, where the dependence between the cell outputs with those of its neighborhood is not directly explained. The NLSC-CNN architecture has been used for several applications, including video and image processing [14–16]. The authors have analyzed the target of robust skin lesion discrimination and, after several optimization tests, designed the following further deep learned features:

$$
A = \begin{bmatrix} 0 & 0 & 0 \\ 0 & 0 & 0 \\ 0 & 0 & 0 \end{bmatrix}; B = \begin{bmatrix} 0.8 & 0.21 & 0.20 \\ 0.20 & 0.71 & 0.20 \\ 0.71 & 0.20 & 0.31 \end{bmatrix}; C = \begin{bmatrix} 0 & 0 & 0 \\ 0 & 0 & 0 \\ 0 & 0 & 0 \end{bmatrix}; D = \begin{bmatrix} 0 & 0.3 & 0 \\ 0.3 & 0 & 0.3 \\ 0 & 0.3 & 0 \end{bmatrix}; I = 0.65 \tag{20}
$$

$$A = \begin{bmatrix} 0 & 0 & 0 \\ 0 & 0 & 0 \\ 0 & 0 & 0 \end{bmatrix}; B = \begin{bmatrix} 0.23 & 0.95 & 0.01 \\ 0.20 & 0.14 & 0.11 \\ 0.23 & 0.20 & 0.20 \end{bmatrix}; C = \begin{bmatrix} 0 & 0 & 0 \\ 0 & 0 & 0 \\ 0 & 0 & 0 \end{bmatrix}; D = \begin{bmatrix} 0 & 0 & 0 \\ 0 & 0 & 0 \\ 0 & 0 & 0 \end{bmatrix}; I = 0.35 \quad (21)$$

$$A = \begin{bmatrix} 0 & 0 & 0 \\ 0 & 0 & 0 \\ 0 & 0 & 0 \end{bmatrix}; B = \begin{bmatrix} 0.18 & 0.20 & 0.20 \\ 0.20 & 0.22 & 0.20 \\ 0.66 & 0.20 & 0.20 \end{bmatrix}; C = \begin{bmatrix} 0 & 0 & 0 \\ 0 & 0 & 0 \\ 0 & 0 & 0 \end{bmatrix}; D = \begin{bmatrix} 0 & 0.1 & 0 \\ 0.1 & 0 & 0.1 \\ 0 & 0.1 & 0 \end{bmatrix}; I = 0.65 \quad (22)$$

$$A = \begin{bmatrix} 0 & 0 & 0 \\ 0 & 0 & 0 \\ 0 & 0 & 0 \end{bmatrix}; B = \begin{bmatrix} 0.13 & 0.35 & 0.13 \\ 0.20 & 0.14 & 0.72 \\ 0.65 & 0.50 & 0.51 \end{bmatrix}; C = \begin{bmatrix} 0.1 & 0.2 & 0 \\ 0 & 0.1 & 0 \\ 0.2 & 0 & 0 \end{bmatrix}; D = \begin{bmatrix} 0 & 0 & 0 \\ 0 & 0 & 0 \\ 0 & 0 & 0 \end{bmatrix}; I = 0.15 \quad (23)$$

$$A = \begin{bmatrix} 0 & 0 & 0 \\ 0 & 0 & 0 \\ 0 & 0 & 0 \end{bmatrix}; B = \begin{bmatrix} 0.22 & 0.44 & 0.32 \\ 0.25 & 0.97 & 0.59 \\ 0.71 & 0.33 & 0.41 \end{bmatrix}; C = \begin{bmatrix} 0.2 & 0 & 0.2 \\ 0 & 0.3 & 0 \\ 0.2 & 0 & 0.2 \end{bmatrix}; D = \begin{bmatrix} 0 & 0 & 0 \\ 0 & 0 & 0 \\ 0 & 0 & 0 \end{bmatrix}; I = 0.35 \quad (24)$$

$$A = \begin{bmatrix} 0 & 0 & 0 \\ 0 & 0 & 0 \\ 0 & 0 & 0 \end{bmatrix}; B = \begin{bmatrix} 0.78 & 0.88 & 0.65 \\ 0.20 & 0.21 & 0.20 \\ 0.33 & 0.45 & 0.41 \end{bmatrix}; C = \begin{bmatrix} 0 & 0 & 0 \\ 0 & 0 & 0 \\ 0 & 0 & 0 \end{bmatrix}; D = \begin{bmatrix} 0 & 0.5 & 0 \\ 0.5 & 0 & 0.5 \\ 0 & 0.5 & 0 \end{bmatrix}; I = 0.25 \quad (25)$$

At the end of the described analysis, we collected 16 hand-crafted features that we arranged in a 32×32 matrix by means of a bi-cubic resizing algorithm [12] as well as six deep learned features generated by the NLS-CNNs properly configured.

In the following Figure 7, the authors report some of the generated features:
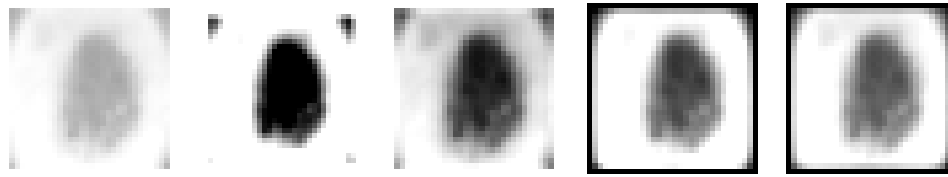
Figure 7. Some instances of the dermoscopic image features generated by a previous block.

2.3. The Deep Learning Classification Block

The goal of this block is the proper classification of features previously described in order to oncologically discriminate the analyzed skin lesion. Specifically, the objective of this part of the proposed pipeline is to discriminate skin lesions—benign (i.e., with a low risk of oncological progression) as compared to malignant (i.e., with a high risk of malign progression).

On the basis of this lesion discrimination and in agreement with the attending physician, the algorithm will provide a follow-up rate for the patient.

In this work, the authors tried to further improve the performance of the previous version of the pipeline [1–3] by using Deep Convolutional Neural Network (ConvNN) architecture for further processing of image features coming from previous blocks. The next sections will explain the structure of the Deep ConvNN that we propose in this work:

- Input Layers $32 \times 32 \times 1$
- Convolution Layer (kernels $3 \times 3 \times 1$, 8-filters, Padding)
- Gradient Normalization Layer
- ReLU Layer
- MaxPooling Layer (2×2)
- Convolution Layer (kernels $3 \times 3 \times 1$, 16-filters, Padding)
- ReLU Layer
- MaxPooling Layer (2×2)

- Convolution Layer (kernels $3 \times 3 \times 1$, 32-filters, Padding)
- ReLU Layer

The proposed pipeline is shown in the following figure:

In Figure 8 the proposed Deep Convolutional Neural Network (ConvNN) architecture is reported. As noticed from the input layer description, the input size is 32×32. Consequently, we resized each dermoscopic image of the analyzed nevi (included in the PH^2 dataset) to a size of 32×32; therefore, the 2D structure of the used NLSC-CNNs will be composed of 32×32 cells having dynamics defined by the cloning templates described in Equations (20)–(25). Furthermore, the described 16 hand-crafted image features had previously been arranged in a 32×32 size pattern, becoming in fact a sort of "morphologic pattern" suitable for identifying each of the analyzed ones. All the described resizing was done using a classical bi-cubic algorithm [12]. In the following paragraphs, each layer of ConvNNs is described:
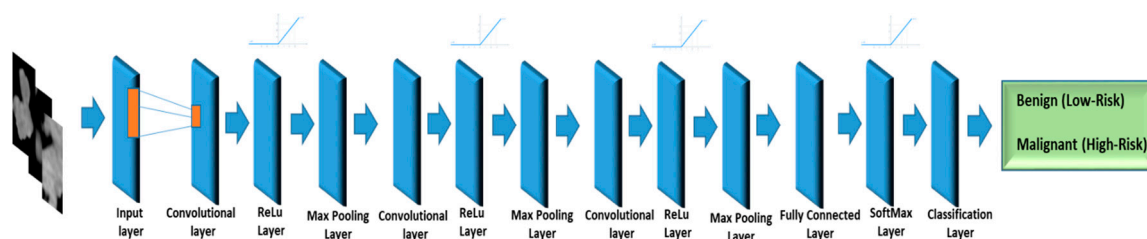

Figure 8. The proposed Deep Convolutional Neural Network pipeline.

Input Layer: These numbers correspond to the height, width, and channel size. As said, the input data (CNNs processed features) consists of grayscale images, so channel size (color channel) is one.

Convolutional Layer: In the convolutional layer, the first argument is filter size, which is the height and width of the kernel filters the training function uses while scanning the CNNs lesion features images. In this case, the number 3 indicates that we have used a filter size of 3-by-3. The second argument is the number of filters, which is the number of neurons that connect to the same region of the input. This parameter determines the dimension of the so-called "feature maps" generated by the ConvNNs.

ReLU Layer: The convolutional layer is followed by a nonlinear activation function. We decided to use the most common activation function i.e., the rectified linear unit (ReLU).

Max Pooling Layer: In the Deep ConvNN paradigm, the convolutional layers (with activation functions) are sometimes followed by a down-sampling operation that reduces the spatial size of the feature map and removes redundant spatial information. The max pooling layer returns the maximum values of rectangular regions of feature input image coming from the previous layer.

The proposed pipeline performs deep learning of the skin lesion image features that come from the previous block and at the end the learned features will be fed into further layers that are part of the overall skin lesion discrimination system, as described:

- Fully-Connected Layer (2 Output Neurons)
- Softmax Layer
- Classification Layer

The following paragraphs describe the above layers:

Fully Connected Layer: This layer combines all the features learned by the previous layers across the image to identify larger patterns. The last fully connected layer combines the features to classify the images. In this case, in the last fully connected layer, we defined the number of classes in the target data i.e., two, as described in the previous section (benign nevus versus malignant ones).

Softmax Layer: The output of the softmax layer consists of positive numbers that sum up to one, which can then be used as classification probabilities by the classification layer.

Classification Layer: The final layer is the classification layer. This layer uses the probabilities returned by the softmax activation function for each input to assign the input to one of the mutually exclusive classes and compute loss and performance indexes. The classification output is further processed by the Autonomous Diagnosis System, which suggests a "follow-up rate" according to the detected oncological risk to be agreed with the attending physician. Specifically, the system will suggest prompt contact with the attending physician if it classifies the analyzed nevus at high risk of malignancy or will suggest a follow-up rate of more than six months if it considers that the analyzed skin lesion is at low risk of oncological progression. Obviously, the physician will be able to decide the follow-up rate on the basis of appropriate medical assessments, which are in fact based on the preventive evaluation performed by the algorithm.

3. Results

The proposed method has been trained and tested by using classified skin lesion images included in a database called "PH^2" [4]. The PH^2 database consists of several dermoscopic images containing benign nevus as well as malignant ones (melanoma) with different morphologic features. The PH^2 dataset has been developed for research purposes and to allow a robust comparison between the methods of discriminative analysis of skin lesions for oncological purposes. The dermoscopic images included in the PH^2 dataset were acquired during daily clinical activity performed at the Dermatology Service of Hospital Pedro Hispano, Matosinhos, Portugal. As reported in the related documentation [4], the dermoscopic images were acquired through the Tuebinger Mole Analyzer system using a magnification of 20×. The dataset contains 8-bit RGB color images with resolution of 768 × 560 pixels. It includes dermoscopic images of melanocytic lesions, including benign lesions (common, atypical and dysplastic nevus) and several cancerous skin lesions (i.e., melanomas) with different morphologies (diameter, asymmetry, edge regularity, etc.). The PH^2 database includes medical annotation of each reported image. The medical diagnosis for each reported lesion was performed by an expert dermatologist. The PH^2 dataset was thus properly organized. About 65% of the PH^2 dataset images were used as a training set. In the training set thus composed, dermoscopic images of benign skin lesions with different morphological features (common, atypical and dysplastic nevus) are included. Moreover, several dermoscopic images of cancerous lesions (melanomas) have been included in the training set but with different characteristics (diameter, edges, regularity of the contours, etc.). Therefore, the used training set consists of about 130 8-bit RGB dermoscopic images of benign and malignant lesions. In this way, we tried to increase the generalization capability of the proposed deep learning system. The remaining set of images (35%) of the PH^2 dataset (also composed of images of benign lesions and melanomas) were used for the testing and validation of the proposed pipeline. In order to provide a robust and efficient benchmarking of the proposed approach, we decided to include a comparison with several similar pipelines validated on the same PH^2 database. In order to perform a fair comparison of the proposed method with respect to other approaches, we evaluated our approach by computing the same benchmark indicators as computed in the compared methods [4]. Specifically, we computed the 'sensibility' indicator as well 'specificity' and cost function '*C*', which can be computed as reported in the following equation:

$$C = \frac{c_{10}(1-SE) + c_{01}(1-SP)}{c_{10} + c_{01}}$$

$$c_{10} = 1.5 : c_{01} = 1$$

The parameter *C* includes the term C_{10} as the weight coefficient of wrong classification (the pipeline classifies "malignant" or high risk a skin lesion, which actually is benign i.e., a false negative FN), while C_{01} represents the weight coefficient for a False Positive (FP) wrong classification (the pipeline classifies "benign" or low-risk a nevus, which actually is malignant or high-risk). From a simple mathematical analysis of the model used for computing *C*, it is clear that the system considers a False Positive more

dangerous with respect to a False Negative for reasons that appear to be easily understandable, because they are linked to the extremely high danger of failure to report a malignant lesion, rather than a wrong classification of benign lesion, which could lead to closer controls and nothing more. Table 1 reports performance benchmark comparison with respect to several approaches applied to the same PH^2 database [17,18]. In Table 2, further performance indicators related to the proposed approach are reported.

Table 1. Benchmarks comparison for the proposed pipeline.
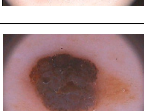
Method [4,16]	Sensitivity	Specificity	C
LM [2]	97%	95%	0.0682
SAE [3]	98.5%	98.1%	0.0166
Proposed	**99.1%**	**98.5%**	**0.0114**
GM (Color)	90%	89%	0.1040
LM (Color)	93%	84%	0.1060
LM (Textures)	88%	76%	0.1680
GF-C6–kNN	**100%**	71%	0.1160
GF-C1–kNN	88%	81%	0.1490
G–AdaBoost	96%	77%	0.117
LF-BoF	98%	79%	0.100

Table 2. Performance measure indicators of the proposed approach.

Method	Accuracy	F1-Score
Proposed	99.00%	99.07%

In Table 3, the authors reported analyzed skin lesions and related classification made by the proposed pipeline.

Table 3. Classified nevus versus classification made by the proposed pipeline.

PH^2 Image	Proposed Pipeline	Classification in PH^2	Follow-Up Rate
	Non-melanoma (Benign Nevus)	Common Nevus (Benign Nevus)	>=6 months
	Non-melanoma (Benign Nevus)	Common Nevus (Benign Nevus)	>=6 months
	Non-melanoma (Benign Nevus)	Dysplastic Nevus (Benign Nevus)	>=6 months
	Melanoma (Cancer lesion)	Melanoma (Cancer lesion)	Contact physician immediately
	Melanoma (Cancer lesion)	Melanoma (Cancer lesion)	Contact physician immediately
	Melanoma (Cancer lesion)	Melanoma (Cancer lesion)	Contact physician immediately

In Table 2, we reported further performance measure indicators, specifically, the accuracy index of the overall pipeline as well as the F1-score (also known as F-measure) [19]. Moreover, we showcased the ROC diagram in Figure 9.
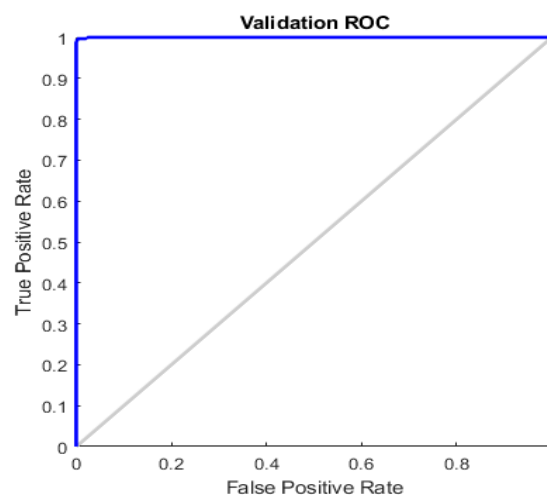

Figure 9. The ROC diagram of the proposed method.

Both from the analysis of the ROC reported in Figure 9 and the common performance indices (Sensitivity, Specificity, F1-score and Accuracy) reported in Tables 1 and 2, it is evident that the proposed method has remarkable capabilities of identification (sensitivity) and discrimination (specificity) of skin lesions. With accuracy close to 100%, the proposed pipeline was able to identify skin lesions at high risk of malignancy, thus allowing the dermatologist/oncologist to promptly schedule treatment. It is possible to verify this by analyzing the malignant lesions present in the PH^2 dataset (used for the training and testing of the proposed method); there are dermoscopic images of cancerous lesions at the limit of the indications in the mentioned ABCDE criterion, which can escape visual inspection by expert physicians (we refer to cases of melanoma with a small diameter or edges not completely irregular). The proposed pipeline was also able to correctly identify malignant lesions, highlighting to the physician the high risk of the nevus, as well as suggesting a follow-up rate. Moreover, in order to avoid unnecessary biopsies, a lot of work has also been done on the discriminative capacity (specificity) of the proposed pipeline. Even in the case of dysplastic or atypical nevus (included both in the training set and in the set of dermoscopic images used for testing/validation) the proposed algorithm was able to correctly characterize the benignity of the lesion by appropriately evaluating the similarity features of the analyzed lesion (thanks to the designed hand-crafted features). The use of the features generated by the convolution system has allowed to significantly improve the specificity of the pipeline proposed compared to the previous versions, as the used ConvNN allowed to extract latent features otherwise not detectable by the classic techniques based on hand-crafted features, which allowed the classifier to properly separate the two classes of skin lesions (benign versus malignant).

4. Discussion and Conclusions

A simple comparison between benchmark results of the methods reported in Tables 1 and 2 shows promising performance of the herein reported method with respect to other similar pipelines, also including the previous version of the same pipeline [1–3]. An innovative combination between re-designed hand-crafted lesion image features with further features generated by the NLSC-CNNs system and innovative Deep Convolutional Neural Network framework considerably improves the overall discrimination performance of the system. As reported in Table 1, it is clear that several approaches proposed in scientific literature increase sensitivity of the pipelines to the disadvantage of 'specificity' or vice versa. Unfortunately, a major drawback of poor skin lesion discrimination

specificity is more nevus biopsy for patients. The proposed approach tries to achieve an excellent trade-off between sensitivity and specificity, thus offering the physician a practical tool that can be used in everyday medical practice. The development of the proposed approach as well as training and validation over the PH^2 database was made in MATLAB 2018b full toolboxes environment with ad-hoc NLSC-Cellular Neural Network functions library. The time performance of the proposed method is acceptable, as the proposed pipeline is able to analyze a single nevus in about 2.5/3 s (we tested the pipeline in a PC Intel Core having 12 Cores 64 Gbyte of RAM and a GPU Nvidia GTX 2030). The proposed pipeline is currently being ported from a MATLAB environment to an embedded platform based on STM32 [19]. We are extending the skin lesions image dataset in order to better validate the discrimination performance of the proposed approach. Moreover, we have been studying the use of physiological signals acquired in the area of the skin lesion to extract ad-hoc dynamic features to be used for nevus classification [20–25] as well as an ad-hoc chemotherapy approach, driven by features detected trough the proposed approach [26]. Specifically, through the innovative approaches used by the authors to characterize physiological signals related to blood-arterial flow activity (including the PhotoPlethysmoGraphic (PPG) signal analysis), we have been analyzing the underlying evolution of skin lesions for early detection of the lymphatic or hematic invasiveness of this lesion because vascular or lymphatic invasion is one of the most discriminating indicators of the malignancy or benignity.

A recent extension of the proposed method is being validated on a larger dataset than the one used in this article, which includes over 10,000 suitably cataloged skin lesions. Specifically, the authors, in addition to using recent deep learning approaches based on convolutive architecture with dilation, are exploiting a particular cross-correlation measure formulated originally by the authors themselves in [27] and now modified to be applied to discriminative analysis of skin lesions. In a future work, the authors aim to describe the preliminary results they have achieved using this innovative approach.

5. Patent

Francesco Rundo, Giuseppe Luigi Banna. Methods and System for Analyzing Skin Lesions, IT Patent Application Number 102016000121060, 29 November 2016—USA Application Number 15607178, 26 May 2017.

References

1. Conoci, S.; Rundo, F.; Petralia, S.; Battiato, S. Advanced skin lesion discrimination pipeline for early melanoma cancer diagnosis towards PoC devices. In Proceedings of the IEEE 2017 European Conference on Circuit Theory and Design (ECCTD), Catania, Italy, 4–6 September 2018.
2. Rundo, F.; Conoci, S.; Banna, G.L.; Stanco, F.; Battiato, S. Bio-Inspired Feed-Forward System for Skin Lesion Analysis, Screening and Follow-Up. In *Image Analysis and Processing—ICIAP 2017*; Lecture Notes in Computer Science (LNCS Including Subseries Lecture Notes in Artificial Intelligence and Lecture Notes in Bioinformatics); Springer International Publishing: Cham, Switzerland, 2017; Volume 10485, pp. 399–409.
3. Rundo, F.; Conoci, S.; Banna, G.L.; Ortis, A.; Stanco, F.; Battiato, S. Evaluation of Levenberg–Marquardt neural networks and stacked autoencoders clustering for skin lesion analysis, screening and follow-up. *IET Comput. Vis.* **2018**, *12*, 957–962. [CrossRef]
4. Mendonça, T.; Ferreira, P.M.; Marques, J.S.; Marcal, A.R.; Rozeira, J. PH^2-A dermoscopic image database for research and benchmarking. In Proceedings of the 35th International Conference of the IEEE Engineering in Medicine and Biology Society, Osaka, Japan, 3–7 July 2013.

5. Sathiya, S.B.; Kumar, S.S.; Prabin, A. A survey on recent computer-aided diagnosis of Melanoma. In Proceedings of the 2014 International Conference on Control, Instrumentation, Communication and Computational Technologies (ICCICCT), Kanyakumari, India, 10–11 July 2014.

6. Xie, F.; Fan, H.; Li, Y.; Jiang, Z.; Meng, R.; Bovik, A. Melanoma Classification on Dermoscopy Images Using a Neural Network Ensemble Model. *IEEE Trans. Med. Imaging* **2017**, *36*, 849–858. [CrossRef] [PubMed]

7. Majtner, T.; Yildirim-Yayilgan, S.; Hardeberg, J.Y. Combining deep learning and hand-crafted features for skin lesion classification. In Proceedings of the Sixth International Conference on Image Processing Theory, Tools and Applications (IPTA), Oulu, Finland, 12–15 December 2016.

8. Guo, Y.; Ashour, A.S.; Si, L.; Mandalaywala, D.P. Multiple Convolutional Neural Network for Skin Dermoscopic Image Classification. In Proceedings of the IEEE International Symposium on Signal Processing and Information Technology (ISSPIT), Louisville, KY, USA, 6–8 December 2018; pp. 365–369.

9. Ayan, E.; Ünver, H.M. Data augmentation importance for classification of skin lesions via deep learning. In Proceedings of the 2018 Electric Electronics, Computer Science, Biomedical Engineerings' Meeting (EBBT), Istanbul, Turkey, 18–19 April 2018; pp. 1–4.

10. Celebi, M.E.; Wen, Q.; Hwang, S.; Iyatomi, H.; Schaefer, G. Lesion border detection in dermoscopy images using ensembles of thresholding methods. *Skin Res. Technol.* **2013**, *19*, e252–e258. [CrossRef] [PubMed]

11. Fukushima, K. Neocognitron: A self-organizing neural network model for a mechanism of pattern recognition unaffected by shift in position. *Biol. Cybern.* **1980**, *36*, 93–202. [CrossRef]

12. Gonzalez, R.C.; Woods, R.E. *Digital Image Processing*, 3rd ed.; Prentice Hall: Upper Saddle River, NJ, USA, 2007.

13. Chua, L.O.; Yang, L. Cellular Neural Networks: Theory. *IEEE Trans. Circuits Syst.* **1988**, *35*, 1257–1272. [CrossRef]

14. Arena, P.; Baglio, S.; Fortuna, L.; Manganaro, G. Dynamics of state controlled CNNs. In Proceedings of the 1996 IEEE International Symposium on Circuits and Systems, Circuits and Systems Connecting the World, ISCAS 96, Atlanta, GA, USA, 15 May 1996.

15. Hagan, M.T.; Menhaj, M. Training feed-forward networks with Marquardt algorithm. *IEEE Trans. Neural Netw.* **1994**, *5*, 989–993. [CrossRef] [PubMed]

16. Duan, S.; Hu, X.; Dong, Z.; Wang, L.; Mazumder, P. Memristor-Based Cellular Nonlinear/Neural Network: Design, Analysis, and Applications. *IEEE Trans. Neural Netw. Learn. Syst.* **2015**, *26*, 1202–1213. [CrossRef] [PubMed]

17. Bengio, Y. Learning Deep Architectures for AI. *Found. Trends Mach. Learn.* **2009**, *2*, 1–127. [CrossRef]

18. Barata, C.; Ruela, M.; Francisco, M.; Mendonça, T.; Marques, J.S. Two Systems for the Detection of Melanomas in Dermoscopy Images using Texture and Color Features. *IEEE Syst. J.* **2013**, *8*, 965–979. [CrossRef]

19. Derczynski, L. Complementarity, F-score, and NLP Evaluation. In Proceedings of the Tenth International Conference on Language Resources and Evaluation (LREC 2016), Portorož, Slovenia, 23–28 May 2016.

20. STM32 32-bit ARM Cortex MCUs. Available online: http://www.st.com/en/microcontrollers/stm32-32-bit-arm-cortexmcus.html?querycriteria=productId=SC1169 (accessed on 1 July 2019).

21. Rundo, F.; Conoci, S.; Ortis, A.; Battiato, S. An Advanced Bio-Inspired PhotoPlethysmoGraphy (PPG) and ECG Pattern Recognition System for Medical Assessment. *Sensors* **2018**, *18*, 405. [CrossRef] [PubMed]

22. Rundo, F.; Ortis, A.; Battiato, S.; Conoci, S. Advanced Bio-Inspired System for Noninvasive Cuff-Less Blood Pressure Estimation from Physiological Signal Analysis. *Computation* **2018**, *6*, 46. [CrossRef]

23. Mazzillo, M.; Maddiona, L.; Rundo, F.; Sciuto, A.; Libertino, S.; Lombardo, S.; Fallica, G. Characterization of sipms with nir long-pass interferential and plastic filters. *IEEE Photonics J.* **2018**, *10*. [CrossRef]

24. Rundo, F.; Petralia, S.; Fallica, G.; Conoci, S. A nonlinear pattern recognition pipeline for PPG/ECG medical assessments. In *Sensors. CNS 2018*; Lecture Notes in Electrical Engineering; Springer International Publishing: Cham, Switzerland, 2019; Volume 539, pp. 473–480.

25. Vinciguerra, V.; Ambra, E.; Maddiona, L.; Romeo, M.; Mazzillo, M.; Rundo, F.; Fallica, G.; di Pompeo, F.; Chiarelli, A.M.; Zappasodi, F.; et al. PPG/ECG multisite combo system based on SiPM technology. In *Sensors. CNS 2018*; Lecture Notes in Electrical Engineering; Springer International Publishing: Cham, Switzerland, 2019; Volume 539, pp. 105–109.

26. Banna, G.L.; Camerini, A.; Bronte, G.; Anile, G.; Addeo, A.; Rundo, F.; Zanghi, G.; Lal, R.; Libra, M. Oral metronomic vinorelbine in advanced non-small cell lung cancer patients unfit for chemotherapy. *Anticancer Res.* **2018**, *38*, 3689–3697. [CrossRef] [PubMed]

27.   Ortis, A.; Rundo, F.; Di Giore, G.; Battiato, S. Adaptive Compression of Stereoscopic Images. In *Image Analysis and Processing—ICIAP 2013*; Lecture Notes in Computer Science; Springer: Berlin/Heidelberg, Germany, 2013; Volume 8156, pp. 391–399.